The Astronomical Journal, 159:115 (9pp), 2020 March https://doi.org/10.3847/1538-3881/ab6e66

Confirmation of WASP-107b's Extended Helium Atmosphere with Keck II/NIRSPEC

James Kirk[1], Munazza K. Alam[1], Mercedes López-Morales[1], and Li Zeng[2]
[1] Center for Astrophysics | Harvard & Smithsonian, 60 Garden Street, Cambridge, MA 02138, USA; james.kirk@cfa.harvard.edu
[2] Department of Earth and Planetary Sciences, Harvard University, Cambridge, MA 02138, USA
Received 2019 August 5; revised 2019 December 17; accepted 2020 January 20; published 2020 February 20

Abstract

We present the detection of helium in the extended atmosphere of the sub-Saturn WASP-107b using high-resolution ($R \approx 25{,}000$) near-infrared spectra from Keck II/Near Infrared Echelle Spectrograph (NIRSPEC). We find peak excess absorption of 7.26% ± 0.24% (30σ) centered on the He I triplet at 10833 Å. The amplitude and shape of the helium absorption profile is in excellent agreement with previous observations of escaping helium from this planet made by CARMENES and the *Hubble Space Telescope*. This suggests there is no significant temporal variation in the signature of escaping helium from the planet over a two year baseline. This result demonstrates Keck II/NIRSPEC's ability to detect atmospheric escape in exoplanets, making it a useful instrument to further our understanding of the evaporation of exoplanetary atmospheres via ground-based observations of He I.

Unified Astronomy Thesaurus concepts: Observational astronomy (1145); Exoplanets (498)

1. Introduction

Recently, Spake et al. (2018) announced the ground-breaking detection of He I in the extended atmosphere of the sub-Saturn exoplanet WASP-107b, using the G102 grism on *Hubble Space Telescope*'s (*HST*) Wide Field Camera 3 (WFC3) instrument. Spake et al. (2018) detected an excess absorption of 0.049% ± 0.011% in a 98 Å wide bin centered on the helium triplet at 10833 Å. This absorption suggested that the planet is losing mass at a rate of 10^{10} –3 × 10^{11} g s^{-1}, or equivalently 0.1%–4% of its total mass per gigayear (Spake et al. 2018).

Prior to the detection by Spake et al. (2018), this absorption signature of a metastable state of neutral helium at 10833 Å had been predicted to be a strong feature in exoplanet transmission spectra (Seager & Sasselov 2000; Turner et al. 2016; Oklopčić & Hirata 2018). However, despite early efforts (Moutou et al. 2003), it went undetected until the detection of Spake et al. (2018).

The result of Spake et al. (2018) coincided with a theoretical study of Oklopčić & Hirata (2018), who generated 1D models of escaping atmospheres and demonstrated that observations of He I absorption could be used as a powerful tool for studying atmospheric escape. This is because it suffers little from extinction, can be observed from the ground, and can probe the escaping planetary wind.

Prior to the detection of helium in WASP-107b's atmosphere, the detections of extended atmospheres had primarily been achieved via studies of Lyα at UV wavelengths (e.g., Vidal-Madjar et al. 2003; Lecavelier Des Etangs et al. 2010; Ehrenreich et al. 2015; Bourrier et al. 2018), which can only be observed with *HST*. These studies have revealed enormous clouds of escaping hydrogen, with absorption depths as large as 56.3% (GJ 436b, Ehrenreich et al. 2015), which have enabled detailed studies of the cloud properties and dynamics (e.g., Bourrier & Lecavelier des Etangs 2013; Bourrier et al. 2016). However, Lyα is strongly affected by both interstellar extinction, limiting observations to planets within ∼50 pc (e.g., Jensen et al. 2018), and contamination from geo-coronal emission (e.g., Ehrenreich et al. 2015).

In addition to studies of Lyα, Hα has also been used as a probe of extended exoplanet atmospheres, with a handful of detections to date (Jensen et al. 2012, 2018; Casasayas-Barris et al. 2018; Yan & Henning 2018). However, this line is more strongly affected by the host star's activity than the metastable helium triplet, where stellar activity is more likely to dilute the signal than to amplify it, making misinterpretation regarding the planetary nature of any absorption less likely (Cauley et al. 2018). This makes the metastable helium triplet attractive for studies of extended atmospheres, even in the case of active host stars (Cauley et al. 2018).

Studies of the helium triplet can therefore provide us with a larger sample of evaporating exoplanets than is currently achievable via observations of Lyα and Hα. This will allow for further constraints to be placed on models of escaping exoplanet atmospheres (Oklopčić & Hirata 2018). By building the sample of exoplanets known to be undergoing atmospheric loss, we can further constrain the role that photoevaporation plays in shaping the population of observed exoplanets. Evaporation is thought to be responsible for the Neptune desert, a region of parameter space where there is a dearth of Neptunian exoplanets (e.g., Mazeh et al. 2016), and the gap in the radius distribution of small planets between 1.5 and 2 Earth radii (Fulton et al. 2017; Owen & Wu 2017; Zeng et al. 2017). The ability to observe evaporation from the ground will allow for robust tests of the role of evaporation in shaping exoplanet populations.

Indeed, there have been six ground-based detections of extended helium atmospheres since the detection of Spake et al. (2018), with one additional space-based detection (Allart et al. 2018, 2019; Mansfield et al. 2018; Nortmann et al. 2018; Salz et al. 2018; Alonso-Floriano et al. 2019; Ninan et al. 2019). However, there have also been four nondetections of extended helium atmospheres (Kreidberg & Oklopčić 2018; Nortmann et al. 2018; Crossfield et al. 2019), with the stellar XUV flux likely playing a key role (Nortmann et al. 2018; Oklopčić 2019).

Here, we present the detection of the extended helium atmosphere of WASP-107b using the high-resolution ($R =$ 25,000) near-infrared spectrograph NIRSPEC on the Keck II telescope. This is the first time this instrument has been used to detect helium in an exoplanet's atmosphere.

WASP-107b, detected by Anderson et al. (2017), is a warm sub-Saturn with a mass of 0.119 M_J, radius of 0.924 R_J, and equilibrium temperature of 736 K (Močnik et al. 2017).

Because of its deep transit (2.09%, Močnik et al. 2017) and large atmospheric scale height (855 km, derived from Močnik et al. 2017), it is an excellent target for atmospheric studies. In addition to the detection of escaping He I (Spake et al. 2018; Allart et al. 2019), Kreidberg et al. (2018) detected water using *HST*/WFC3's G141 grism and found evidence for a methane-depleted atmosphere and high-altitude condensates.

2. Observations

We observed a single transit of the planet WASP-107b on the night of 2019 April 6 using the Near Infrared Echelle Spectrograph (NIRSPEC) on the Keck II telescope at Maunakea Observatory, Hawai'i. We acquired 36 spectra of the target over $3^{h}51^{m}$ of observations, which covered an airmass ranging from 1.97 to 1.16 and were approximately centered on the time of mid-transit given by the ephemeris of Močnik et al. (2017).

Our observations were taken using an ABBA nod pattern to improve sky subtraction, meaning that nod pairs needed to be combined during the data reduction, as described in Section 3. We used the $0.432 \times 12''$ slit with an exposure time of 300 s, other than for eight frames during ingress where an exposure time of 400 s was used. This was because of a drop in counts, which was caused by the slit wheel inadvertently changing to a narrower, $0''.144$ wide slit for five frames. The slit change occurred during an AB nod pair, which was removed from further analysis due to the different resolution of the A and B nods. This left us with 34 spectra of the target (17 nod pairs), with four frames taken with the narrower slit (data points 6 and 7 in the light curve, Figure 6).

We acquired observations of a telluric standard A0 star prior to the transit of WASP-107b, but chose to use ESO's molecfit (Kausch et al. 2015; Smette et al. 2015) to perform the telluric correction, as described in Section 3. We also acquired halogen lamp flats and NeArKrXe arcs, which were used in the data reduction as described in Section 3.

3. Data Reduction

All of the observed data were reduced using the IDL-based REDSPEC software package[3] (McLean et al. 2003, 2007). The package performs standard bad pixel interpolation, removal of fringing effects, and flat fielding, as well as spatial rectification of curved spectra. We focused our reduction on NIRSPEC order 70, which contains the He I triplet at 10833 Å and covers a wavelength range of 10799–11014 Å. The spectra were rectified and extracted in differenced nod pairs so that the sky background and OH emission lines were removed. Aperture photometry was performed to extract the spectra, with an aperture width of 11 pixels.

Following the extraction of the spectra, we used iSpec[4] (Blanco-Cuaresma et al. 2014; Blanco-Cuaresma 2019) to perform the continuum normalization of the spectra and to cut the ends of the spectra where the counts dropped significantly, leaving a usable wavelength range of 10800–10975 Å. As mentioned in Section 2, two of our nod pairs were taken with a narrower, $0''.144$ slit. At this stage we used iSpec to degrade the resolution of these spectra to a resolution of 25,000, in line with the rest of our data.

To wavelength calibrate our data, we began with the Ar, Ne, Kr, and Xe arc lamp lines taken at the start of the observations. However, we found that this resulted in wavelength solutions that deviated from the truth by $\approx 5\,\mathrm{km\,s^{-1}}$ (less than half NIRSPEC's resolution of $12\,\mathrm{km\,s^{-1}}$), with deviations that differed by a couple of $\mathrm{km\,s^{-1}}$ across the order, indicating a distorted wavelength dispersion.

To correct these effects, we used stellar and telluric atmosphere models to refine the wavelength solution. For the stellar atmosphere model, we used a PHOENIX model (Husser et al. 2013), which we degraded to the resolution of NIRSPEC ($R = 25{,}000$) using iSpec. The PHOENIX model had an effective temperature of 4400 K, surface gravity ($\log g$) of 4.5 cgs, and metallicity ([Fe/H]) of 0.0, as close to the parameters of WASP-107 as possible ($T_{\rm eff} = 4430$ K, $\log g = 4.5$, $[\mathrm{Fe/H}] = +0.02$; Anderson et al. 2017).

For the telluric model, we used a synthetic telluric spectrum generated for Maunakea with 1.0 mm precipitable water vapor at an airmass of 1.5, which we obtained from the Gemini Observatory's web pages.[5] This model had a wavelength spacing of $\Delta\lambda = 0.2$ Å, approximately twice that of our NIRSPEC data. We scaled this model to roughly match the amplitude of the telluric features in our observed spectra. This model was only used for wavelength calibration refinement and not for telluric removal, which is described later in this section.

We applied a barycentric velocity correction to each extracted spectrum using the Astropy library (Astropy Collaboration et al. 2013) in Python and applied a systemic velocity and stellar reflex velocity correction to the PHOENIX model, which was convolved with the telluric spectrum for each frame. This resulted in a model containing stellar and telluric absorption lines which was used to refine the wavelength correction of each observed spectrum in turn. Since the He I triplet is a chromospheric line, it did not appear in the PHOENIX model we used and so the wavelength refinement was not affected by the He I absorption of the planet.

To perform the wavelength refinement, we split the spectra into eight separate chunks, which were evenly spaced in wavelength, and cross-correlated each of these with the model using iSpec. It was necessary to split the spectra into chunks for cross-correlation due to the distortion of the wavelength solution across the order. This resulted in the radial velocity of each chunk as a function of wavelength, which we fitted with a cubic polynomial to refine the wavelength dispersion and solution.

Then with the wavelength-corrected extracted spectra in the barycentric frame, we used ESO's molecfit (Kausch et al. 2015; Smette et al. 2015) to perform the telluric correction. We chose not to use the telluric standard star to perform the telluric removal as the telluric standard was only observed prior to our observations of WASP-107. Since our science observations covered a broad range of airmass, we found that our limited standard star spectra did not adequately remove the telluric absorption from our science spectra.

Molecfit uses Global Data Assimilation System[6] profiles that contain weather information for user-specified observatory coordinates, airmasses, and times. It then models the telluric

[3] https://www2.keck.hawaii.edu/inst/nirspec/redspec.html
[4] https://www.blancocuaresma.com/s/iSpec
[5] http://www.gemini.edu/sciops/telescopes-and-sites/observing-condition-constraints/ir-transmission-spectra#0.9-2.7um
[6] https://www.ncdc.noaa.gov/data-access/model-data/model-datasets/global-data-assimilation-system-gdas

Table 1
The System Parameters of WASP-107b Used in the Data Reduction and Analysis

Parameter	Symbol	Value	Reference
Time of mid-transit	T_0	2457584.329746 BJD	Močnik et al. (2017)
Orbital period	P	5.72149242 day	Močnik et al. (2017)
Orbital inclination	i	89.°560	Močnik et al. (2017)
White-light scaled planet radius	R_p/R_*	0.142988	Spake et al. (2018)
Semimajor axis	a	0.0553 au	Močnik et al. (2017)
Scaled semimajor axis	a/R_*	18.10	Močnik et al. (2017)
Stellar mass	M_*	0.691 $M_\odot$	Močnik et al. (2017)
Planet mass	M_p	0.119 M_J	Močnik et al. (2017)
Planet radius	R_p	0.924 R_J	Močnik et al. (2017)
Semi-amplitude	K_*	16.45 m s^{-1}	Allart et al. (2019)
Systemic velocity	γ	13.74 km s^{-1}	Gaia DR2 (Gaia Collaboration et al. 2016, 2018)

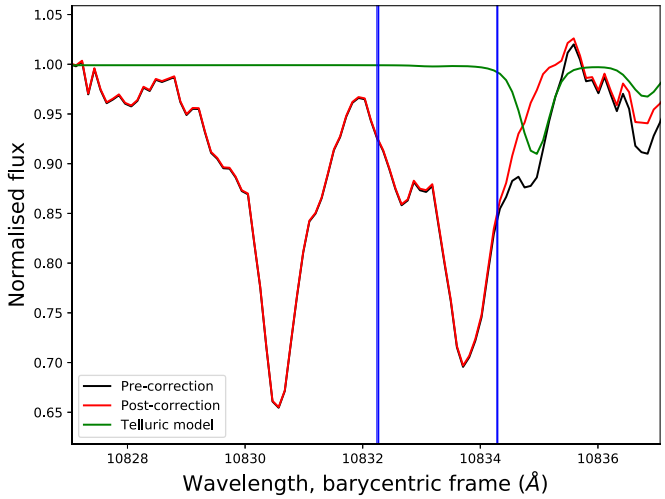

Figure 1. Result of the telluric removal performed using molecfit (Kausch et al. 2015; Smette et al. 2015). The spectrum before and after the correction is shown in black and red, respectively. The green line shows the telluric absorption model. The location of OH emission lines, which are corrected for by the AB pair subtraction (see the text), are shown by the blue vertical lines.

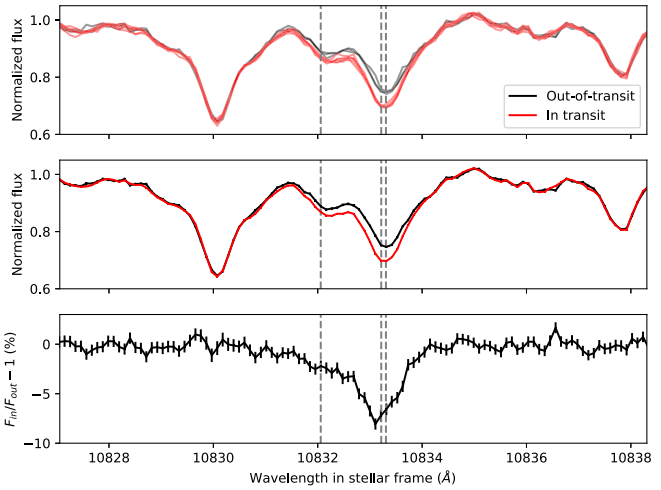

Figure 2. Top panel: the individual nod pair spectra of WASP-107. Out-of-transit spectra are shown in black with the in-transit spectra shown in red. This reveals a clear signal of in-transit absorption around the helium triplet, which is shown by the dashed vertical lines. Middle panel: the master co-added nod pair spectra, with out-of-transit shown in black and in-transit spectra shown in red. Bottom panel: the master in-transit spectrum divided by the master out-of-transit spectrum, which reveals the excess absorption by WASP-107b's atmosphere in the region of the helium triplet.

absorption lines in the observed spectra using this information. We found that a choice of nine telluric absorption lines, free of significant stellar absorption, allowed molecfit to perform a good removal of the telluric absorption from our spectra. We chose to fit only for the atmospheric H_2O content, with CH_4 and O_2 fixed. Figure 1 shows an example spectrum before and after the telluric correction using molecfit. This figure demonstrates that while OH emission and telluric absorption lines sit near the helium triplet lines (which have wavelengths in vacuo of 10832.1, 10833.2, and 10833.3 Å), the core of the triplet is unaffected.

With the tellurics removed we then shifted the spectra into the stellar rest frame, using the system parameters given in Table 1. We subsequently created master in- and out-of-transit spectra to allow us to study the in-transit absorption by He I. Initially we used the ephemeris of Močnik et al. (2017) to determine which spectra were taken in- and out-of-transit. However, due to the longer duration of the transit at the He I triplet we had to use our own light curve (as discussed in Section 5) to determine which phase each spectrum corresponded to. This resulted in three pre/out-of-transit spectra, four ingress spectra, six in-transit spectra, and four egress spectra. We combined our three pre-transit and six in-transit spectra into master out-of-transit and in-transit spectra, respectively.

4. Data Analysis

Figure 2 shows the resulting master in- and out-of-transit spectra, in the stellar rest frame. This figure clearly indicates the excess absorption centered on the helium triplet during the planet's transit, which reaches a level of over 7%.

To generate the transmission spectrum and light curve of WASP-107b, we first had to calculate the residual spectra for each frame by dividing each frame by the master out-of-transit spectrum. Figure 3 shows the plot of the excess absorption in the stellar frame as a function of the planet's orbital phase. The dashed white lines indicate the planet's velocity and show that the wavelength of the absorption is consistent with the planetary motion for the majority of the transit but deviates during egress. This could indicate the presence of material trailing the planet, which is being blown away. However, further observations are needed to confirm this feature and hypothesis.

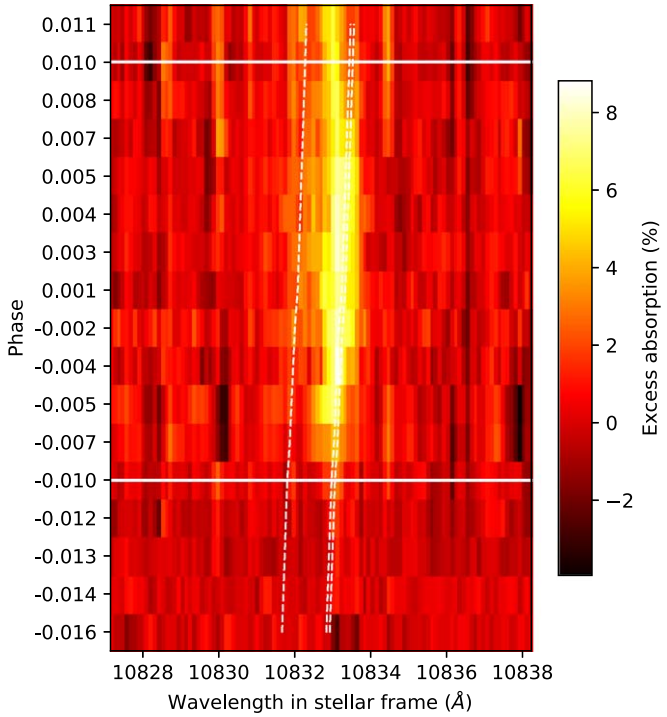

Figure 3. Excess absorption by metastable helium during the transit of WASP-107b shown on a plot of orbital phase vs. wavelength. The dashed white lines indicate the planet's orbital motion at the wavelengths of the helium triplet. The horizontal white lines indicate the ingress and egress phases from the white light curve of Spake et al. (2018). Note that the *y*-axis is not evenly spaced in phase.

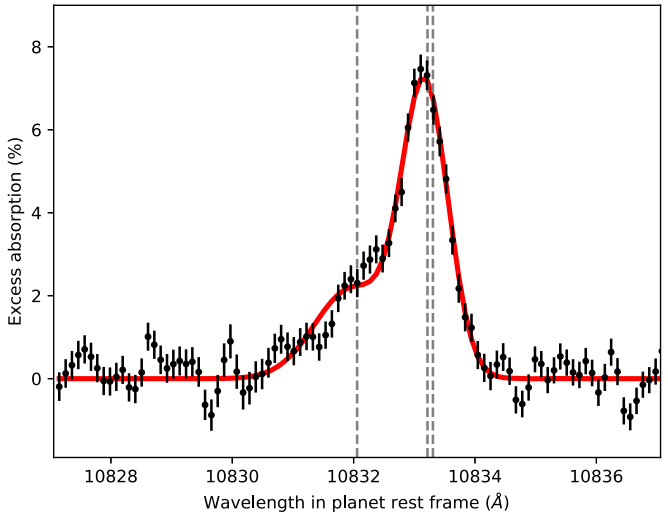

Figure 4. Excess absorption during transit, in the planet's rest frame. The vertical dashed lines indicate the locations of the helium triplet and the red line shows a fit of a double-peaked Gaussian to this absorption profile, which resulted in a peak absorption of 7.26% ± 0.24% during transit. The centers of the Gaussians are blueshifted by −2.35 ± 0.39 km s^{-1}.

By shifting the excess absorption to the planet's rest frame, we were able to construct the He I transmission spectrum of the planet, which is shown in Figure 4. This transmission spectrum resulted in a peak excess absorption of 7.26 ± 0.24% during transit. We fitted this absorption profile with the summation of two Gaussians using a nonlinear least-squares fit using the Scipy Python module (Jones et al. 2001). We fitted for the standard deviations and amplitudes of the two components, along with a wavelength offset which allowed the means of the two Gaussians to deviate from the locations of the absorption wavelengths of the He I triplet. This was necessary owing to the small blueshift that was apparent in the peak's location (Figure 4), as also noted by Allart et al. (2019). This resulted in an amplitude for the first and second Gaussian components of 2.17% ± 0.14% and 6.95% ± 0.21%, respectively. This gave a ratio between the two components of 3.2, which deviates from the optically thin ratio of 8 (e.g., de Jager et al. 1966; Salz et al. 2018). The fitted offset was −0.085 ± 0.014 Å, or equivalently a blueshift of −2.35 ± 0.39 km s^{-1}. This blueshift indicates that material is being blown away from the planet, in agreement with the findings of Allart et al. (2019; Figure 5).

Furthermore, we are able to compare our transmission spectrum with that of Allart et al. (2019) who used the Calar Alto high-Resolution search for M dwarfs with Exoearths with Near-infrared and optical Échelle Spectrographs (CARMENES; Quirrenbach et al. 2014) on the 3.5 m telescope at Calar Alto (Figure 5). This figure demonstrates the excellent agreement between our result and that of Allart et al. (2019), both in terms of the amplitude and shape of the transmission spectrum. Figure 5 also shows that a resolution of 25,000 is sufficient to resolve the amplitude of the He I absorption. Allart et al. (2019) additionally degraded their spectrum to the resolution of the *HST*/WFC3 spectrum of Spake et al. (2018) and found excellent agreement with their data. The three studies of the helium absorption of WASP-107b (Spake et al. 2018; Allart et al. 2019 and this work) therefore indicate that the signal is nonvariable over the two year baseline of these studies.

Figure 6 shows the absolute light curve constructed by multiplying the excess absorption in the planet's rest frame by a light curve with the same R_P/R_* as the white light curve of Spake et al. (2018). Our light curve was constructed using a 0.43 Å region centered on the mean of the redder two lines of the helium triplet (10833.26 Å). We fitted this absolute light curve with an analytic transit light curve using the Batman Python module (Kreidberg 2015), using a nonlinear limb-darkening law with the coefficients fixed to the values used by Spake et al. (2018). We fixed the inclination (i), scaled semimajor axis (a/R_*), period (P), and transit mid-point (T_0) to the values in Table 1. We fitted for R_P/R_* only, which we again did using a nonlinear least-squares fit through the Scipy Python module (Jones et al. 2001). This resulted in an $R_P/R_* = 0.2759 \pm 0.0025$, which is 1.93× the white light R_P/R_* of Spake et al. (2018).

Figure 6 also shows the excess transit duration that we observed at the core of the He triplet as compared with the near-infrared continuum. To determine the extra duration, we resampled our He light curve model and the near-infrared light curve model at a cadence of 30 s. The difference in the first and fourth contact points between the two models amounted to an excess transit duration of 19 minutes observed in the He line core. This compares to an excess transit duration of 30 minutes observed by Allart et al. (2019) in a 0.75 Å-wide bin. However, given our little out-of-transit coverage, our extra duration should be considered a lower limit, while Allart et al. (2019) had better coverage of the transit.

4.1. Stellar Variability

In this section we consider what effect the intrinsic stellar variability of WASP-107 has on our result (Figure 4).

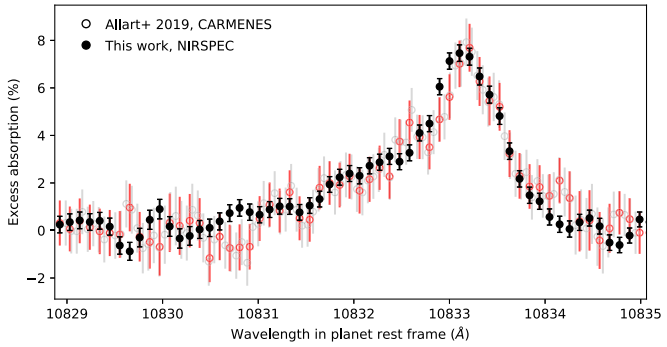

Figure 5. Excess absorption during transit in the planet's rest frame. The results of this work are shown by the filled black circles. The results from the study of Allart et al. (2019) using CARMENES are shown by the open circles, with the gray points at the resolution of CARMENES ($R = 80{,}400$; Quirrenbach et al. 2018) and the red points at the resolution of NIRSPEC ($R = 25{,}000$).

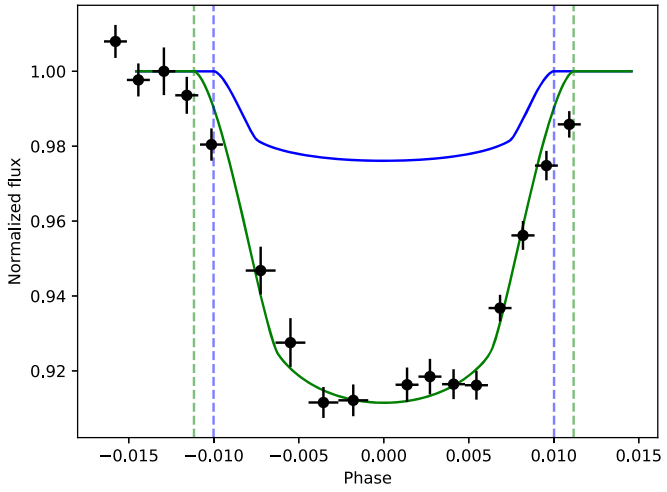

Figure 6. Absolute helium light curve integrated from 10833.05 to 10833.48 Å (black error bars) and following the multiplication by the white light curve of Spake et al. (2018). The green line shows the transit light curve fitted to our observations, with the blue line showing the white light curve of Spake et al. (2018). The R_P/R_* of our He light curve is 1.93× the white light value of Spake et al. (2018). The vertical dashed blue and green lines indicate the ingress and egress phases of the white light curve of Spake et al. (2018) and our He light curve, respectively. We measure a longer transit duration at the location of the He triplet, with a lower limit on the extra duration of 19 minutes.

For optical data in particular, stellar activity can lead to deeper or shallower transit depths depending on the temperature of the active region in relation to the photosphere, and whether this activity lies along or away from the planet's transit chord (e.g., McCullough et al. 2014; Oshagh et al. 2014; Kirk et al. 2016; Rackham et al. 2017; Alam et al. 2018).

Anderson et al. (2017) used Wide Angle Search for Planets (WASP) photometry, acquired in 2009 and 2010, to measure the photometric modulation of WASP-107. They found WASP-107 to modulate with a period of 17 days and an amplitude of 0.4%. Spake et al. (2018) performed a similar analysis using ground-based photometric monitoring of WASP-107 from MEarth (Nutzman & Charbonneau 2008) and Automated Imaging Telescope (AIT; Henry 1999). From these two instruments, both covering approximately 4 months in 2017, the authors detected modulations of 0.0015 and 0.005 mag with periods of 19.7 and 8.675 days, respectively. Spake et al. (2018) found that a heterogeneous photosphere with a spot covering fraction of 8^{+6}_{-3}% and faculae covering fraction of 53^{+15}_{-12}% could lead to the 0.4% variation found by Anderson et al. (2017).

Cauley et al. (2018) simulated the transit of a planet across an active host star and measured the changes in atomic lines sensitive to the stellar chromosphere, including He I at 10833 Å. They simulated a number of different scenarios, changing the overall activity level of the star and the latitude of the activity with respect to the planet's transit chord. The maximum spot and faculae[7] covering fractions they considered were 10% and 50%, respectively, similar to the covering fractions for WASP-107 found by Spake et al. (2018). Cauley et al. (2018) showed that He I absorption at 10833 Å can be contaminated at the 0.1% level (far smaller than the 7.26% absorption we detect; Figure 4). Also, depending on the location of this activity, it can actually lead to a dilution of the planet's absorption signal rather than an enhancement.

Furthermore, given that the amplitude of the absorption is consistent over a baseline of 2 yr (Spake et al. 2018; Allart et al. 2019), it is unlikely that stellar activity, which is inherently variable, could produce such consistency. The above reasons indicate that the absorption we detect (Figure 4) is planetary in nature and is not significantly influenced by stellar activity.

4.1.1. The Rossiter–McLaughlin Effect

The Rossiter–McLaughlin (Rossiter 1924; McLaughlin 1924) effect can lead to spurious velocity shifts if not correctly accounted for in the planet's frame. However, it has less of an effect in the stellar frame where the Rossiter–McLaughlin effect is near-symmetric (e.g., Louden & Wheatley 2015). In the case of our observations, the small blueshifted absorption we observe is present in both the stellar rest frame (Figure 2) and the planet's rest frame (Figure 4).

Since WASP-107b is a slow rotator ($v \sin i = 2.5 \pm 0.8$ km s^{-1}; Anderson et al. 2017), the predicted amplitude of the Rossiter–McLaughlin effect is expected to be small (Dai & Winn 2017). Indeed, using Equation (5) of Dai & Winn (2017), with the R_P/R_* we calculate from our He light curve in Section 4, we find that the expected signal amplitude is 133 m s^{-1}. This is an order of magnitude smaller than the blueshift we observe (Figure 4) and two orders of magnitude smaller than the resolution of NIRSPEC. We therefore do not expect our results to be impacted by the Rossiter–McLaughlin effect.

5. Discussion

5.1. WASP-107b's Extended Helium Atmosphere

This is the third paper that presents the detection of the extended helium atmosphere of WASP-107b, confirming the results of Spake et al. (2018) and Allart et al. (2019). We find that the planet's radius is 1.93× larger at the location of the helium triplet than the surrounding continuum (Section 4, Figures 4 and 6). This amounts to approximately half the Roche-lobe radius of 3.34 R_P, using the approximation of Eggleton (1983) and planet parameters given in Table 1.

The helium absorption profile of Allart et al. (2019) showed a blueshifted excess, indicating a tail of escaping material. They modeled this absorption using the 3D EVaporating

[7] Note that Cauley et al. (2018) included chromospheric plage in their definition of faculae.

Table 2
Sample of 11 Planets Predicted to Show Extended Helium Atmospheres

	$T_{\rm eff}$ (K)	$T_{\rm eq}$ (K)	Escape Velocity (km s^{-1})[a]	$\log_{10}(-\Phi_{\rm G})n$ (erg g^{-1})[a]	Semimajor axis (au)	J mag.[b]	Transit Depth per H (ppm)[a]	Reference
HAT-P-12b	4665	955	27.8	12.59	0.03767	10.8	342	Mancini et al. (2018)
HAT-P-18b	4870	841	27.1	12.56	0.0559	10.8	303	Esposito et al. (2014)
HAT-P-26b	5011	1001	19.2	12.27	0.0479	10.1	211	Hartman et al. (2011)
Qatar-1b	4910	1418	63.3	13.30	0.02332	11.0	109	Collins et al. (2017)
Qatar-6b	5052	1006	47.2	13.05	0.0423	9.7	148	Alsubai et al. (2018)
TOI-216b	5026	628	20.0	12.30	0.1293	10.8	182	Kipping et al. (2019)
WASP-11b	4900	992	42.0	12.94	0.04375	10.0	140	Mancini et al. (2015)
WASP-29b	4875	970	33.4	12.75	0.04565	9.4	122	Gibson et al. (2013)
WASP-52b	5000	1315	35.0	12.79	0.02643	10.6	413	Mancini et al. (2017)
WASP-80b	4145	825	44.9	13.00	0.03479	9.2	171	Mancini et al. (2014)
WASP-177b	5017	1142	33.8	12.76	0.03957	10.7	484	Turner et al. (2019)

Notes.
[a] Derived parameter using values from studies in the reference column.
[b] Two Micron All Sky Survey magnitudes (Skrutskie et al. 2006).

Exoplanet code (EVE; Bourrier & Lecavelier des Etangs 2013; Bourrier et al. 2016) and found that their simulations were consistent with helium escaping at the exobase with a thermal wind velocity of $\sim$12 km s^{-1}.

The shape of the excess absorption by He I we detect is very similar to that seen by Allart et al. (2019; Figure 5). Similar to that study, we also detect a blueshifted excess (Figure 4), which we measure to have an amplitude of -2.35 ± 0.39 km s^{-1}. This is further evidence for a wind of material escaping the planet, following the conclusions of Spake et al. (2018) and Allart et al. (2019). We also detect non-Keplerian, blueshifted absorption during WASP-107b's egress (Figure 3), which could correspond to material trailing the planet. However, additional observations are needed to confirm this feature.

Given the absence of any post-transit, and only a short pre-transit baseline, we can only place a lower limit on the excess transit duration at the location of the helium triplet (Figure 6). The excess transit duration we observe is 19 minutes, as compared with the white light transit of Spake et al. (2018). Our He I light curve also appears symmetric about the mid-point (Figure 6), similar to what was found by Spake et al. (2018) and Allart et al. (2019). However, we note that our lack of post-transit baseline does not allow us to constrain the presence of post-transit absorption.

5.2. Keck/NIRSPEC as an Instrument for Exoplanetary He I Observations

Our study is the third ground-based high-resolution spectrograph used to detect the helium triplet in an exoplanet's atmosphere. This follows the use of CARMENES (Quirrenbach et al. 2014) and the Habitable Zone Planet Finder (HPF; Mahadevan et al. 2014; Metcalf et al. 2019) near-infrared spectrograph on the 10 m Hobby–Eberly Telescope, which have together made similar detections in six other exoplanets (Allart et al. 2018, 2019; Nortmann et al. 2018; Salz et al. 2018; Alonso-Floriano et al. 2019; Ninan et al. 2019).

The resolutions of CARMENES ($R \approx 80{,}400$) and HPF ($R \approx 55{,}000$) are both higher than NIRSPEC ($R \approx 25{,}000$). This offers advantages with respect to detecting the blueshifted absorption profile expected to be associated with an escaping wind of material. However, Figure 5 demonstrates that a resolution of 25,000 is sufficient to resolve the absorption's amplitude and shape for WASP-107b. Additionally, Keck II's 10 m aperture does provide a significant advantage in terms of the signal-to-noise ratio over the 3.5 m telescope at Calar Alto Observatory that is home to CARMENES. This is highlighted in Figure 5, which shows the higher precision that we were able to achieve with our Keck observations, as compared to Allart et al. (2019). Our demonstration is promising for the search for helium signatures around smaller planets, where the higher precision will be more important than resolution in the search for these smaller signals.

5.3. Predicting Promising Exoplanets for Observations of He I

In addition to WASP-107b (Spake et al. 2018; Allart et al. 2019; this work) extended helium atmospheres have been detected for the hot Jupiters HD 189733b (Salz et al. 2018) and HD 209458b (Alonso-Floriano et al. 2019), the Saturn-mass planet WASP-69b (Nortmann et al. 2018), and the Neptunes HAT-P-11b (Allart et al. 2018; Mansfield et al. 2018) and GJ 3470b (Ninan et al. 2019). Four of these exoplanets orbit K stars while the remaining two orbit G and M stars. Oklopčić (2019) suggested that K stars have the necessary XUV (EUV and X-ray) to mid-UV flux ratios to maintain a populated metastable helium state in the atmospheres of these exoplanets, as EUV ionizes the helium ground state, populating the metastable state, while mid-UV ionizes the helium metastable state. This makes K-star hosts the most favorable targets for detecting exoplanetary metastable helium. Similarly, Nortmann et al. (2018) showed that the exoplanets with helium detections orbit stars with higher activity levels and receive greater levels of XUV radiation than the exoplanets with nondetections.

In addition to the host's spectral type, both the gravitational potential and semimajor axis of the planet are predicted to influence the atmospheric escape (Salz et al. 2016b; Nortmann et al. 2018; Oklopčić 2019).

In Table 2 we present 11 known exoplanets that are promising targets for future observations of extended helium atmospheres. To derive this list, we took the sample of well-studied transiting planets from TEPCat[8] (Southworth 2011) and

[8] https://www.astro.keele.ac.uk/jkt/tepcat/

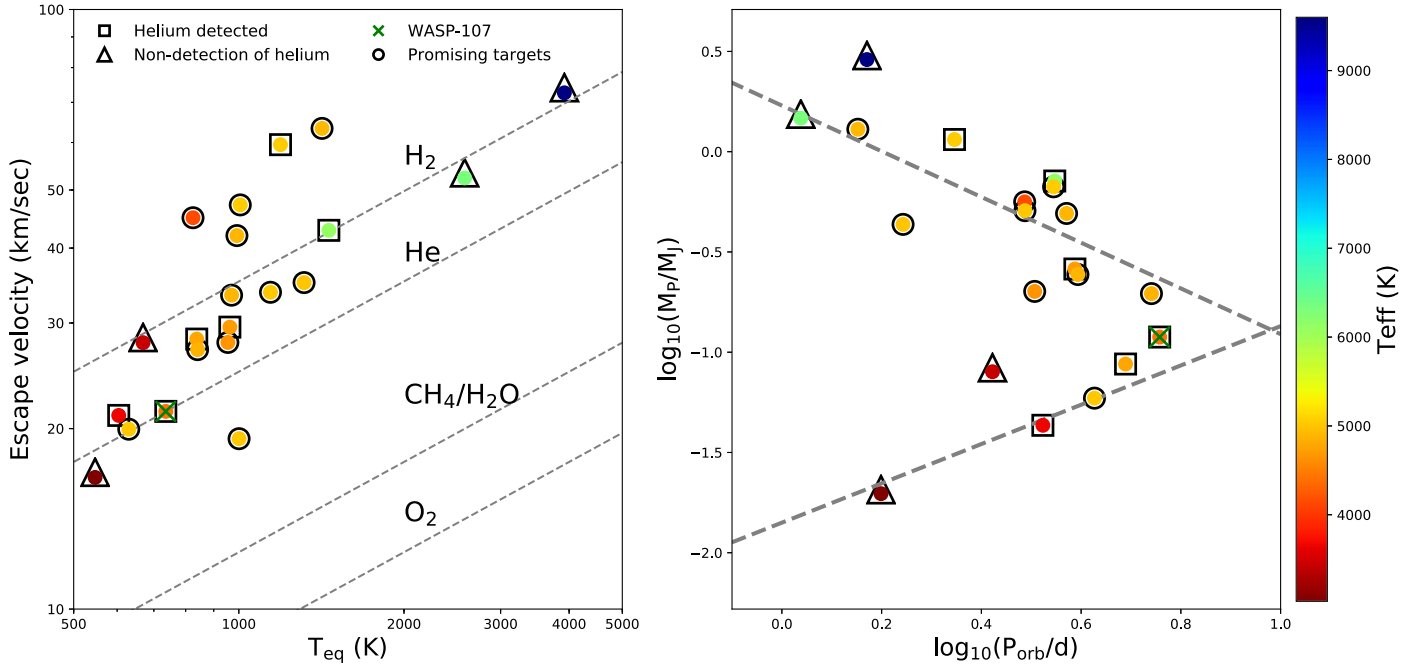

Figure 7. Left panel: a plot of planet escape velocity against equilibrium temperature for exoplanets with confirmed He I detections (black squares), nondetections (black triangles), and the sample of exoplanets that we have identified as promising targets for helium observations (black circles). WASP-107b is highlighted by the green cross. All the plotted exoplanets are colored by the effective temperatures of their host stars. The gray dashed lines indicate the threshold escape limits for various gas compositions considering thermal escape (Jeans escape). Planets falling below a given line are expected to be losing that gas. Note: the temperature in the escaping zone (upper atmosphere) of the envelope may be higher than the estimated equilibrium temperature of the planet, due to absorption of UV photons by various gas species and UV-driven photochemistry. However, the equilibrium temperature can be considered a lower bound. Right panel: the same sample of planets as shown in the left panel but shown in mass–period space. The dashed gray lines indicate the extent of the Neptune desert, as defined by Mazeh et al. (2016).

selected planets that have bloated radii, which lead to large transit depths per scale height (δ) of >100 ppm, calculated through

$$\delta = \frac{2HR_p}{R_*^2}, \quad (1)$$

where H is the atmospheric scale height, and R_P and R_* are the radii of the planet and star, respectively. We then kept only those planets that orbit relatively bright ($J \leqslant 11$) K stars ($4000 \leqslant T_{\rm eff} \leqslant 5100$ K).

We also note that the gravitational potentials of 10 of these planets fall within the hydrodynamic wind regime of Salz et al. (2016b; $\log_{10}(-\Phi_G) < 13.2$), while Qatar-1b sits in an intermediate region where hydrodynamic escape can exist but is suppressed (Salz et al. 2016a).

In Table 2 we also include the semimajor axes of this sample, as Nortmann et al. (2018) and Oklopčić (2019) showed that helium absorption depends on the orbital separation. Oklopčić (2019) suggested that semimajor axes between ~0.03 and 0.1 au are optimal for observations of helium in exoplanets orbiting main-sequence stars.

Figure 7 (left panel) plots the escape velocity of this sample of planets against their equilibrium temperatures, with the mean velocity of various gases overplotted. Any planet sitting below a certain line is susceptible to losing that gas via Jeans escape. This demonstrates that hydrodynamic escape is dominating for the sample of planets with detected helium absorption, as they all sit above the line where helium would be lost via Jeans escape.

We also plot this sample of planets in mass–period space (Figure 7, right panel), along with the boundaries of the Neptune desert as defined by Mazeh et al. (2016). The 11 exoplanets in Table 2 sample this space well, and observations of He I could add further constraints on how this desert formed, whether it be via atmospheric loss driven by stellar XUV radiation (e.g., Allan & Vidotto 2019), Roche-lobe overflow (e.g., Matsakos & Königl 2016), or a combination of the two (e.g., Kurokawa & Nakamoto 2014). A better understanding of the processes shaping the Neptune desert might help with the interpretation of the radius gap between 1.5 and 2 Earth radii (Fulton et al. 2017).

6. Conclusions

We have detected He I at 10833 Å in the extended atmosphere of WASP-107b, using Keck II/NIRSPEC. The excess absorption we detect has a peak amplitude of $7.26\% \pm 0.24\%$ and is blueshifted by -2.35 ± 0.39 km s^{-1}. We also see evidence for non-Keplerian, blueshifted absorption during the planet's egress, which could be the result of material trailing the planet. This is further confirmation of WASP-107b's extended helium atmosphere, which is being actively lost, following the findings of Spake et al. (2018) and Allart et al. (2019).

The amplitude and shape of the helium absorption profile we detect are in excellent agreement with the CARMENES results of Allart et al. (2019), who in turn demonstrated consistency with the original *HST* detection of Spake et al. (2018). Our result, when taken together with those of Spake et al. (2018) and Allart et al. (2019), demonstrates that the helium absorption of WASP-107b does not show temporal variability over the baseline of these three studies. We measure an R_P/R_* that is 1.93× the white light value of Spake et al. (2018) and a transit duration that is a minimum of 19 minutes longer. We are unable to put a strong constraint on the extra transit duration owing to our short out-of-transit baseline.

This is the first time Keck II/NIRSPEC has been used to detect helium in an exoplanet atmosphere, demonstrating its capability to probe the upper atmospheres of highly irradiated exoplanets. NIRSPEC now joins CARMENES and HPF as ground-based high-resolution spectrographs that have detected exoplanetary helium at 10833 Å. The seven ground-based detections of this line demonstrate its accessibility to such instruments, while the rate of these detections offers exciting prospects for understanding exoplanet evaporation, and its role in carving such features as the Neptune desert (e.g., Mazeh et al. 2016) and radius gap (Fulton et al. 2017), across a large sample of planets.

7. Software and Third Party Data Repository Citations

We are grateful to the anonymous referee whose comments led to a significant improvement in the manuscript. We are also grateful to Romain Allart for sharing the CARMENES transmission spectrum of WASP-107b, and to Antonija Oklopcic for useful discussions regarding NIRSPEC and the interpretation. Finally we also wish to thank our support astronomer, Greg Doppmann, for guidance during the reduction stage.

The data presented herein were obtained at the W. M. Keck Observatory, which is operated as a scientific partnership among the California Institute of Technology, the University of California and the National Aeronautics and Space Administration. The Observatory was made possible by the generous financial support of the W. M. Keck Foundation. The authors wish to recognize and acknowledge the very significant cultural role and reverence that the summit of Maunakea has always had within the indigenous Hawaiian community. We are most fortunate to have the opportunity to conduct observations from this mountain.

Facility: Keck(NIRSPEC).

Software: Astropy (Astropy Collaboration et al. 2013), Batman (Kreidberg 2015), iSpec (Blanco-Cuaresma et al. 2014; Blanco-Cuaresma 2019), Matplotlib (Hunter 2007), Molecfit (Kausch et al. 2015; Smette et al. 2015), Numpy (Van Der Walt et al. 2011), REDSPEC (McLean et al. 2003, 2007), Scipy (Jones et al. 2001).

ORCID iDs

James Kirk https://orcid.org/0000-0002-4207-6615
Munazza K. Alam https://orcid.org/0000-0003-4157-832X
Mercedes López-Morales https://orcid.org/0000-0003-3204-8183
Li Zeng https://orcid.org/0000-0003-1957-6635

References

Alam, M. K., Nikolov, N., López-Morales, M., et al. 2018, AJ, 156, 298
Allan, A., & Vidotto, A. A. 2019, MNRAS, 490, 3760
Allart, R., Bourrier, V., Lovis, C., et al. 2018, Sci, 362, 1384
Allart, R., Bourrier, V., Lovis, C., et al. 2019, A&A, 623, A58
Alonso-Floriano, F. J., Snellen, I. A. G., Czesla, S., et al. 2019, A&A, 629, A110
Alsubai, K., Tsvetanov, Z. I., Latham, D. W., et al. 2018, AJ, 155, 52
Anderson, D. R., Collier Cameron, A., Delrez, L., et al. 2017, A&A, 604, A110
Astropy Collaboration, Robitaille, T. P., Tollerud, E. J., et al. 2013, A&A, 558, A33
Blanco-Cuaresma, S. 2019, MNRAS, 486, 2075
Blanco-Cuaresma, S., Soubiran, C., Heiter, U., & Jofré, P. 2014, A&A, 569, A111
Bourrier, V., & Lecavelier des Etangs, A. 2013, A&A, 557, A124
Bourrier, V., Lecavelier des Etangs, A., Ehrenreich, D., et al. 2018, A&A, 620, A147
Bourrier, V., Lecavelier des Etangs, A., Ehrenreich, D., Tanaka, Y. A., & Vidotto, A. A. 2016, A&A, 591, A121
Casasayas-Barris, N., Pallé, E., Yan, F., et al. 2018, A&A, 616, A151
Cauley, P. W., Kuckein, C., Redfield, S., et al. 2018, AJ, 156, 189
Collins, K. A., Kielkopf, J. F., & Stassun, K. G. 2017, AJ, 153, 78
Crossfield, I. J. M., Barman, T., Hansen, B., & Frewen, S. 2019, RNAAS, 3, 24
Dai, F., & Winn, J. N. 2017, AJ, 153, 205
de Jager, C., Namba, O., & Neven, L. 1966, BAN, 18, 128
Eggleton, P. P. 1983, ApJ, 268, 368
Ehrenreich, D., Bourrier, V., Wheatley, P. J., et al. 2015, Natur, 522, 459
Esposito, M., Covino, E., Mancini, L., et al. 2014, A&A, 564, L13
Fulton, B. J., Petigura, E. A., Howard, A. W., et al. 2017, AJ, 154, 109
Gaia Collaboration, Brown, A. G. A., Vallenari, A., et al. 2018, A&A, 616, A1
Gaia Collaboration, Prusti, T., de Bruijne, J. H. J., et al. 2016, A&A, 595, A1
Gibson, N. P., Aigrain, S., Barstow, J. K., et al. 2013, MNRAS, 428, 3680
Hartman, J. D., Bakos, G. Á., Kipping, D. M., et al. 2011, ApJ, 728, 138
Henry, G. W. 1999, PASP, 111, 845
Hunter, J. D. 2007, CSE, 9, 90
Husser, T. O., Wende-von Berg, S., Dreizler, S., et al. 2013, A&A, 553, A6
Jensen, A. G., Cauley, P. W., Redfield, S., Cochran, W. D., & Endl, M. 2018, AJ, 156, 154
Jensen, A. G., Redfield, S., Endl, M., et al. 2012, ApJ, 751, 86
Jones, E., Oliphant, T., Peterson, P., et al. 2001, SciPy: Open source scientific tools for Python, http://www.scipy.org/
Kausch, W., Noll, S., Smette, A., et al. 2015, A&A, 576, A78
Kipping, D., Nesvorný, D., Hartman, J., et al. 2019, MNRAS, 486, 4980
Kirk, J., Wheatley, P. J., Louden, T., et al. 2016, MNRAS, 463, 2922
Kreidberg, L. 2015, PASP, 127, 1161
Kreidberg, L., Line, M. R., Thorngren, D., Morley, C. V., & Stevenson, K. B. 2018, ApJL, 858, L6
Kreidberg, L., & Oklopčić, A. 2018, RNAAS, 2, 44
Kurokawa, H., & Nakamoto, T. 2014, ApJ, 783, 54
Lecavelier Des Etangs, A., Ehrenreich, D., Vidal-Madjar, A., et al. 2010, A&A, 514, A72
Louden, T., & Wheatley, P. J. 2015, ApJL, 814, L24
Mahadevan, S., Ramsey, L. W., Terrien, R., et al. 2014, Proc. SPIE, 9147, 91471G
Mancini, L., Esposito, M., Covino, E., et al. 2015, A&A, 579, A136
Mancini, L., Esposito, M., Covino, E., et al. 2018, A&A, 613, A41
Mancini, L., Southworth, J., Ciceri, S., et al. 2014, A&A, 562, A126
Mancini, L., Southworth, J., Raia, G., et al. 2017, MNRAS, 465, 843
Mansfield, M., Bean, J. L., Oklopčić, A., et al. 2018, ApJL, 868, L34
Matsakos, T., & Königl, A. 2016, ApJL, 820, L8
Mazeh, T., Holczer, T., & Faigler, S. 2016, A&A, 589, A75
McCullough, P. R., Crouzet, N., Deming, D., & Madhusudhan, N. 2014, ApJ, 791, 55
McLaughlin, D. B. 1924, ApJ, 60, 22
McLean, I. S., McGovern, M. R., Burgasser, A. J., et al. 2003, ApJ, 596, 561
McLean, I. S., Prato, L., McGovern, M. R., et al. 2007, ApJ, 658, 1217
Metcalf, A. J., Anderson, T., Bender, C. F., et al. 2019, Optica, 6, 233
Močnik, T., Hellier, C., Anderson, D. R., Clark, B. J. M., & Southworth, J. 2017, MNRAS, 469, 1622
Moutou, C., Coustenis, A., Schneider, J., Queloz, D., & Mayor, M. 2003, A&A, 405, 341
Ninan, J. P., Stefansson, G., Mahadevan, S., et al. 2019, arXiv:1910.02070
Nortmann, L., Pallé, E., Salz, M., et al. 2018, Sci, 362, 1388
Nutzman, P., & Charbonneau, D. 2008, PASP, 120, 317
Oklopčić, A. 2019, ApJ, 881, 133
Oklopčić, A., & Hirata, C. M. 2018, ApJL, 855, L11
Oshagh, M., Santos, N. C., Ehrenreich, D., et al. 2014, A&A, 568, A99
Owen, J. E., & Wu, Y. 2017, ApJ, 847, 29
Quirrenbach, A., Amado, P. J., Caballero, J. A., et al. 2014, Proc. SPIE, 9147, 91471F
Quirrenbach, A., Amado, P. J., Ribas, I., et al. 2018, Proc. SPIE, 10702, 107020W
Rackham, B., Espinoza, N., Apai, D., et al. 2017, ApJ, 834, 151
Rossiter, R. A. 1924, ApJ, 60, 15
Salz, M., Czesla, S., Schneider, P. C., et al. 2018, A&A, 620, A97
Salz, M., Czesla, S., Schneider, P. C., & Schmitt, J. H. M. M. 2016a, A&A, 586, A75
Salz, M., Schneider, P. C., Czesla, S., & Schmitt, J. H. M. M. 2016b, A&A, 585, L2
Seager, S., & Sasselov, D. D. 2000, ApJ, 537, 916

Skrutskie, M. F., Cutri, R. M., Stiening, R., et al. 2006, AJ, 131, 1163
Smette, A., Sana, H., Noll, S., et al. 2015, A&A, 576, A77
Southworth, J. 2011, MNRAS, 417, 2166
Spake, J. J., Sing, D. K., Evans, T. M., et al. 2018, Natur, 557, 68
Turner, J. D., Christie, D., Arras, P., Johnson, R. E., & Schmidt, C. 2016, MNRAS, 458, 3880
Turner, O. D., Anderson, D. R., Barkaoui, K., et al. 2019, MNRAS, 485, 5790
Van Der Walt, S., Colbert, S. C., & Varoquaux, G. 2011, CSE, 13, 22
Vidal-Madjar, A., Lecavelier des Etangs, A., Désert, J. M., et al. 2003, Natur, 422, 143
Yan, F., & Henning, T. 2018, NatAs, 2, 714
Zeng, L., Jacobsen, S. B., Hyung, E., et al. 2017, LPI, 48, 1576